

Your Interlibrary Loan request has been sent by email in a PDF format.

If this PDF arrives with an incorrect OCLC status, please contact lending located below.

Concerning Copyright Restrictions

The copyright law of the United States (Title 17, United States Code) governs the making of photocopies or other reproductions of copyrighted materials. Under certain conditions specified in the law, libraries and archives are authorized to furnish a photocopy or other reproduction. One of these specified conditions is that the photocopy or reproduction is not to be "used for any purpose other than private study, scholarship, or research". If a user makes a request for, or later uses, a photocopy or reproduction for purpose in excess of "fair use", that user may be liable for copyright infringement. This institution reserves the right to refuse to accept a copying order if, in its judgment, fulfillment of the order would involve violation of copyright law.

Interlibrary Loan Services: We Search the World for You...and Deliver!

Interlibrary Loan Services
The Florida State University
711 West Madison Street
Tallahassee, Florida 32306-1005

Lending the FSU Collection: 850.644.4171
James Elliott- ILL- lend@reserves.lib.fsu.edu

Borrowing for the FSU Community: 850.644.4466
Alicia Brown- ill@reserves.lib.fsu.edu

Odyssey: 128.186.59.120 Ariel: 146.201.65.22
Fax: 850.644.3329



Discrete multicomponent model for biodiesel spray combustion simulation



M.F. Mohd Yasin^{a,b,*}, R.S. Cant^a, C.T. Chong^b, S. Hochgreb^a

^a Fakulti Kejuruteraan Mekanikal, Universiti Teknologi Malaysia, Malaysia

^b Department of Engineering, University of Cambridge, United Kingdom

HIGHLIGHTS

- Discrete and continuous multicomponent liquid models are calculated from the real biodiesel properties.
- Continuous multicomponent liquid model is employed for diesel spray simulation.
- The predicted spray-combustion characteristics of diesel and biodiesel are compared with the experimental measurements.
- The discrete model performs better than the continuous model in predicting the spray-combustion characteristics of the biodiesel flame.
- Effects of the relative abundance and the relative volatility of biodiesel fuel components are highlighted.

ARTICLE INFO

Article history:

Received 13 May 2013

Received in revised form 10 February 2014

Accepted 11 February 2014

Available online 28 February 2014

Keywords:

Multicomponent

Biodiesel

Spray

Simulation

CFD

ABSTRACT

An important first step in spray combustion simulation is an accurate determination of the fuel properties which affects the modelling of spray formation and reaction. In a practical combustion simulation, the implementation of a multicomponent model is important in capturing the relative volatility of different fuel components. A Discrete Multicomponent (DM) model is deemed to be an appropriate candidate to model a composite fuel like biodiesel which consists of four components of fatty acid methyl esters (FAME). In this paper, the DM model is compared with the traditional Continuous Thermodynamics (CTM) model for both diesel and biodiesel. The CTM model is formulated based on mixing rules that incorporate the physical and thermophysical properties of pure components into a single continuous surrogate for the composite fuel. The models are implemented within the open-source CFD code OpenFOAM, and a semi-quantitative comparison is made between the predicted spray-combustion characteristics and optical measurements of a swirl-stabilised flame of diesel and biodiesel. The DM model performs better than the CTM model in predicting a higher magnitude of heat release rate in the top flame brush region of the biodiesel flame compared to that of the diesel flame. Using both the DM and CTM models, the simulation successfully reproduces the droplet size, volume flux, and droplet density profiles of diesel and biodiesel. The DM model predicts a longer spray penetration length for biodiesel compared to that of diesel, as seen in the experimental data. Also, the DM model reproduces a segregated biodiesel fuel vapour field and spray in which the most abundant FAME component has the longest vapour penetration. In the biodiesel flame, the relative abundance of each fuel component is found to dominate over the relative volatility in terms of the vapour species distribution and vice versa in the liquid species distribution.

© 2014 Elsevier Ltd. All rights reserved.

1. Introduction

Growing interest in biodiesel as a renewable fuel has triggered many studies to understand the spray-combustion characteristics of the new fuel. Application of biodiesel in unmodified engines

requires similar combustion characteristics to those of conventional fuel. Experiments have suggested that differences in fuel physical and chemical properties lead to different spray characteristics such as droplet size [1–3], spray penetration [4], and spray cone angle [5]. Changes in combustion behaviour in terms of emissions [1–3,6], burning velocity [1,7], flame temperature [9], and flame height [6] are observed by switching from conventional fuel to biodiesel. Simulating the differences in spray-combustion characteristics of different fuels is a challenge that requires an

* Corresponding author at: Fakulti Kejuruteraan Mekanikal, Universiti Teknologi Malaysia, Malaysia. Tel.: +6075557035.

E-mail address: mfm38@cam.ac.uk (M.F. Mohd Yasin).

Nomenclature

<i>air</i>	air parameter	<i>V</i>	volume flux
$\bar{}$	averaged quantity	<i>U</i>	velocity
<i>atom</i>	atomising air parameter	\wedge	normalised parameter
<i>z</i>	axial location		
<i>z</i>	axial parameter		
<i>b</i>	biodiesel parameter, boiling parameter	<i>acronym</i>	
<i>ch</i>	characteristic parameter	CFD	Computational Fluid Dynamics
<i>I</i>	chemiluminescence intensity	CTM	Continuous Thermodynamics Model
<i>d</i>	diameter	CTRZ	central top reaction zone
<i>d</i>	diesel parameter, droplet parameter	DM	discrete multicomponent model
ρ	density	FAME	fatty acid methyl esters
<i>N</i>	droplet number	GC	Gas Chromatography
ϕ	equivalence ratio	IDEA	Integrated Diesel European Action
<i>ith</i>	fuel component properties	IDEA-CTM	IDEA with Continuous Thermodynamics Model
\dot{q}	heat release rate per unit volume	OpenFOAM	Open Source Field Operation and Manipulation
<i>q</i>	heat release rate	PSR	Perfectly Stirred Reactor
<i>i</i>	<i>ith</i> computational parcel properties	PaSR	Partially Stirred Reactor
<i>inject</i>	injection parameter	PDA	Phase Doppler Anemometry
<i>m</i>	mass	PISO	Pressure Implicit Split Operator
\dot{m}	mass flow rate	PIV	Particle Image Velocimetry
<i>Y</i>	mass fraction	PME	Palm Methyl Ester
<i>max</i>	maximum variable	PME-CTM	
<i>r</i>	radius		Palm Methyl Ester with Continuous Thermodynamics Model
<i>r</i>	radial parameter	PME-DM	Palm Methyl Ester with Discrete Model
δ	Rosin–Rammler characteristic droplet diameter	TAB	Taylor Analogy Breakup
<i>swirl</i>	swirl air parameter	URANS	Unsteady Reynolds Average Navier Stokes
D_{32}	Sauter mean diameter		
<i>T</i>	temperature		
D_{30}	volume mean diameter		

evaluation of the sensitivity of available (CFD) tools towards fuel properties, and this point is discussed in the present study.

Much work has been done on the effects of the fuel chemical properties in spray combustion modelling [11,12,20] but there are relatively few studies on the effects of the fuel physical properties [14,17]. Before employing a complex and expensive chemistry calculation, the effects of the fuel physical properties need to be understood. The present study decouples the effects of chemistry by comparing models for the liquid fuel properties using an identical chemical mechanism for all fuels considered. Therefore, the effects of the liquid physical properties on spray-combustion characteristics can be studied systematically in isolation.

Different experimental [10,15] and numerical studies [16,34–36] have concentrated on the importance of evaporation in the spray combustion process. Modelling the spray formation and evaporation of practical fuels requires the implementation of a multicomponent model to capture the relative volatility effects. Two approaches have been used in the implementation of multicomponent models, known as the Discrete Multicomponent (DM) model [34,36] and the Continuous Thermodynamics (CTM) model [12,20,35]. The DM model represents each pure component discretely while the CTM model combines all the pure components properties into a single continuous surrogate. Most fossil fuels are modelled with the CTM approach due to its modelling simplicity. Hundreds of components are simplified by a few representative surrogates in the calculation of the pure component properties before the application of mixing rules to formulate a single continuous set of physical properties.

In the case of a composite fuel like biodiesel that consists of only four main fatty acid methyl ester (FAME) components [25], DM is a practical modelling approach. However, many biodiesel computational studies have been done based on the traditional CTM approach [12,20,35] due to the simplicity of the modelling,

which may not be appropriate for biodiesel. A DM approach has been applied to bio-oil evaporating spray [35] and a similar approach has been applied to model decane-heptane evaporating spray [36]. Both of these studies were based on a non-reacting spray, but the present study is intended to observe the effect of combustion on the multicomponent spray formation process. The importance of the relative volatility of different components in the predicted fuel vapour fields has been considered previously [35]. The present study extends the discussion based on a reacting case to illustrate the competition between the relative volatility and the relative abundance of the fuel components in the predicted spray and combustion behaviour.

Prediction methods for FAME pure components have been developed and validated recently, aimed at further studies of biodiesel using the DM method [37]. The CTM method [12,20] involves some compromise on the accuracy of the volatility properties due to the implementation of mixing rules on a composite fuel like biodiesel. A well-established (GC) dataset [25] on biodiesels derived from palm oil, Palm Methyl Esters (PME), is incorporated in the DM model.

Validation of spray combustion simulations has been a limitation on their usefulness [31] due to the complex interplay between different physical processes. Therefore, validation studies of unsteady spray combustion simulations have been limited to macro-scale characteristics such as spray penetration, spray shape, flame shape and global droplet size [19,20]. Validation of the micro-scale characteristics such as local droplet size, droplet flux, and velocity profiles have been limited to sprays of a single component fuel [24]. Hence, the present study aims to validate the same micro-scale spray characteristics for practical fuels. Since there is no validation effort for the multicomponent model that extends to reacting sprays, the present study provides a semi-quantitative validation of the spray and combustion characteristics that

compares spray flames of different fuels. An experimental database of the spray-combustion characteristics of diesel and biodiesel flames [1,2] is used.

The present study compares the predicted biodiesel spray-combustion characteristics based on the DM and CTM models with those of diesel flames modelled using a CTM model called (IDEA). The accuracy of the models is then evaluated based on experimental measurements from a swirl stabilised burner.

In the next section, the experimental setting, the formulation of the liquid model, the spray combustion modelling, and the development of the Lagrangian post-processing approach will be explained. The analysis of the results will follow, and finally the predicted biodiesel spray-combustion characteristics obtained from the DM model will be analysed.

2. Experimental setup

In the experiment, a swirl stabilised burner is employed as shown in Fig. 1. An axial swirler produces swirling air to stabilise the flame and a plain air blast atomiser (Delavan: SN type-30610-1) supplies the fuel. The operating pressure is atmospheric. Table 1 summarises the operating conditions of the biodiesel and diesel swirl stabilised flame. Droplet size and velocity measurements are obtained using (PDA) at 10 mm, 15 mm, and 20 mm downstream of the nozzle. Measurements of gas velocity using (PIV) are taken on a plane passing through the centreline of the spray and sampled at 10 mm, 20 mm, 30 mm, and 40 mm downstream. Imaging using OH* chemiluminescence is taken as an indicator of the heat release rate per unit volume. The same experimental configuration is used for diesel flames and biodiesel flames by fixing the fuel mass flow rate, \dot{m}_{fuel} and maintaining the global equivalence ratio, ϕ . A detailed discussion of the measurement procedures is given in Refs. [1,2].

3. Numerical conditions

3.1. OpenFOAM spray combustion solver

The simulations are carried out using the open-source (CFD) toolbox OpenFOAM. An (URANS) spray combustion solver called

Table 1

Experimental conditions of the reacting spray with a fixed fuel mass flow rate [1,2]

Diesel flame swirl air mass flow rate, $\dot{m}_{swirl,d}$	4.14 g/s
Biodiesel flame swirl air mass flow rate, $\dot{m}_{swirl,b}$	3.44 g/s
Atomising air mass flow rate, \dot{m}_{atom}	0.28 g/s
Fuel mass flow rate, \dot{m}_{fuel}	0.14 g/s
Total power output, \dot{W}	6 kW
Equivalence ratio, ϕ	0.47
Swirl air temperature, T_{swirl}	350 °C
Atomising air temperature, T_{atom}	20 °C
Fuel temperature, T_{fuel}	20 °C

Table 2

Estimation methods and mixing rules that are applied for the fuel physical properties calculation for the PME-CTM and PME-DM models [13,37]. The symbols ρ , σ , μ , p_v , and h_l denote density, surface tension, viscosity, vapour pressure, thermal conductivity, and latent heat of vaporisation respectively.

Properties	PME-CTM (mixing rule)	PME-DM
ρ	Rackett	Rackett
σ	Macleod–Sugden (Raoult's Law)	Corresponding State
μ	Vogel (Grunberg–Nissan)	Orrick & Erbar
p_v	Antoine (Raoult's Law)	Lee Kesler
h_l	Pitzer	Pitzer

dieselFOAM is employed. The standard solver includes an Eulerian–Lagrangian two phase formulation in which the dispersed phase is treated using a Lagrangian approach and the continuous phase is treated using an Eulerian approach. In the spray modelling, droplets with similar properties are represented by a computational parcel which is tracked from the location of injection until the location of the final evaporation. A two-way coupling between the two phases is implemented using momentum, species, and energy source terms in their respective transport equations. An Euler implicit time integration method is employed together with the (PISO) velocity–pressure coupling procedure. A standard $k - \epsilon$ turbulence model is used and the turbulence–chemistry interaction is represented using the (PaSR) model [27]. This model is derived from the (PSR) model and includes the effect of mixing time scale, τ_{mix} and chemical time scale, τ_c . The effects of chemistry are decoupled by using an identical 2-step heptane reaction mechanism [28] for all of the different fuel spray

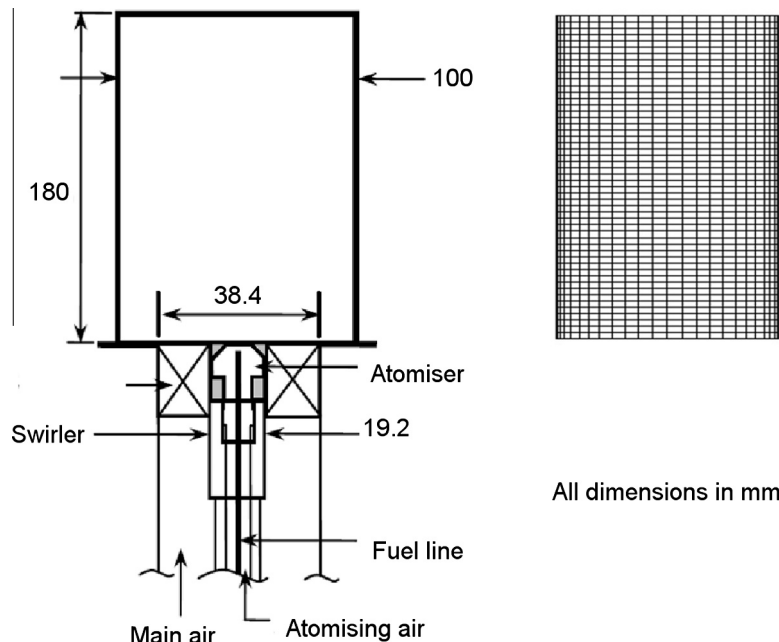


Fig. 1. Left: schematic diagram of the swirl stabilised burner used in the experiment [1,2], right: computational mesh.

Table 3

C₇H₁₆ 2-step reaction mechanism as implemented in the present simulation. The rate constant $k = AT^n \exp(-E/RT)$ where A , n , E , R and T are pre-exponential factor, temperature exponent, activation energy, universal gas constant, and temperature respectively. Units are in cm, mole, and sec [28].

Reaction	A	n	E
C ₇ H ₁₆ + 7.5O ₂ → 7CO + 8H ₂ O	5.0×10^8	0.0	15780.0
CO + 0.5O ₂ + H ₂ O ⇌ CO ₂ + H ₂ O	3.98×10^{14}	0.0	40000.0

simulations as shown in Table 3. Different spray models are implemented for drag, collision, dispersion, and heat transfer [27].

3.2. Evaporation model: The CTM and the DM models

In the present study, the droplet evaporation process is modelled using the D² model which assumes a quasi-steady spherically symmetric isolated droplet. The model is summarised by Eq. (1) in which D , t and C_e are the droplet diameter, time, and evaporation constant respectively.

$$\frac{dD^2}{dt} = C_e \quad (1)$$

$$\frac{dm_d}{dt} = -\pi D Sh \mathcal{D} \rho_v \ln \left(\frac{p - p_{v,\infty}}{p - p_v} \right) \quad (2)$$

$$= -\pi D Sh \mathcal{D} \rho_v \ln \left(1 + \frac{X_v - X_{v,\infty}}{1 - X_v} \right) \quad (3)$$

$$\rho_v = \frac{p_v}{RT_f} \quad (4)$$

$$T_f = \frac{2T_d + T}{3} \quad (5)$$

The CTM evaporation model is implemented in the standard OpenFOAM solver as shown in Eqs. (2) and (3) where variables p , $p_{v,\infty}$, p_v , $X_{v,\infty}$, X_v , Sh , ρ_v and \mathcal{D} are gas pressure, far field vapour pressure, vapour pressure on the droplet surface, far field fuel vapour mass fraction, fuel vapour mass fraction at the droplet surface, Sherwood number, vapour density at the droplet surface, and mass diffusion coefficient respectively. The vapour density at the droplet surface is calculated using the ideal gas law as shown in Eq. (4) where R is the universal gas constant. Assuming a droplet with uniform internal temperature, the film temperature T_f is evaluated using the 1/3rd rule as shown in Eq. (5) where T_d and T are the droplet temperature and the gas temperature respectively.

The Sherwood number is defined based on the Ranz-Marshall correlation as shown in Eq. (6) and the Schmidt number Sc is defined in Eq. (7).

$$Sh = 2.0 + 0.6 Re_d^{1/2} Sc^{1/3} \quad (6)$$

$$Sc = \frac{\mu}{\rho_v \mathcal{D}} \quad (7)$$

The Reynolds number is defined in Eq. (8) where variables \mathbf{u}_d , \mathbf{U} , and μ are the droplet velocity, gas phase velocity, and gas dynamic viscosity respectively. In the OpenFOAM numerical implementation, Eq. (3) is solved using the evaporation relaxation time τ_e as shown in Eq. (9).

$$Re_d = \frac{\rho_v |\mathbf{u}_d - \mathbf{U}| D}{\mu} \quad (8)$$

$$\tau_e = \frac{\rho_d D^2}{6 D Sh \rho_v \ln \left(1 + \frac{X_v - X_{v,\infty}}{1 - X_v} \right)} \quad (9)$$

The DM model represents each pure fuel component as a discrete entity. In the dispersed phase, the mass percentage and evaporation rate of each pure component are modelled based on the measured fuel composition of the real fuel and the calculated

vapour pressure respectively. Every fuel component mass transfer is modelled separately in the spray mass equation. Eq. (2) is modified to Eq. (10) so that each fuel component i evaporates at a different rate based on the i th component vapour pressure, p_{vi} mass diffusivity \mathcal{D}_i , and vapour density ρ_{vi} . The discrete component properties are used to calculate the component i Sherwood number Sh_i . The component i density ρ_{vi} is calculated the same way as Eq. (4) but the component i vapour pressure p_{vi} is used instead of the mixture vapour pressure p_v . Each additional fuel component involves an additional computation of the evaporation rate equation which enables the relative evaporation rate of different fuel components to be modelled.

$$\frac{dm_{di}}{dt} = -\pi D Sh_i \mathcal{D}_i \rho_{vi} \ln \left(\frac{p - p_{vi,\infty}}{p - p_{vi}} \right) \quad (10)$$

In the gas phase, the transport of pure components through diffusion and convection is calculated by a separate partial differential equation for each component. Therefore, the DM model is able to capture the differences in the evaporation and the mixing behaviour of different fuel components that are governed by the relative volatility and the relative abundance of the pure components.

3.3. Fuel properties calculation

The present study implements two liquid models to represent biodiesel: the Palm Methyl Ester with DM model (PME-DM) and the Palm Methyl Ester with CTM model (PME-CTM). Diesel is represented using a CTM model (IDEA). Both the PME-CTM and the IDEA models are treated as single component models. The modelled composition of IDEA consists of 30% alpha naphthalene and 70% n-decane by mass and is readily available in the standard OpenFOAM liquid library [29].

The pure component mass percentage distributions that are implemented in the PME-CTM and the PME-DM models are shown in Table 4. The PME-CTM composition is the same as the (PME) composition that is published in the literature based on the (GC) analysis [25] while the PME-DM composition does not include methyl laurate (C12:0) and methyl myristate (C14:0) due to their small mass percentage relative to the rest of the components. This is necessary to optimise the computation time and the simplification is justified since the mass percentage for C12:0 and C14:0 is less than 2%. The most abundant component in the mixture composition is C16:0 which comprises almost half of the total mass percentage of PME. The PME-CTM approach implements a single surrogate by applying mixing rules over six FAME components.

The PME-CTM properties are calculated using a code called BDProp [13]. Table 2 shows the specific correlations and mixing rules that are implemented in BDProp to calculate various physical properties of biodiesel [13]. In the BDProp calculation, the (GC) analysis of the PME composition, the measured density, and the measured normal boiling point [25] are used as input. Recommended methods [22] are used for the thermal conductivity calculation. The Lagrange polynomials interpolation method and

Table 4

The mass percentage distribution of fuel components in the PME-CTM and the PME-DM models.

Liquid model	PME-CTM (% mass)	PME-DM (% mass)
C12:0 (C ₁₃ H ₂₆ O ₂)	0.267	Omitted
C14:0 (C ₁₅ H ₃₀ O ₂)	1.434	Omitted
C16:0 (C ₁₇ H ₃₄ O ₂)	46.13	46.00
C18:0 (C ₁₉ H ₃₈ O ₂)	3.684	37.00
C18:1 (C ₁₉ H ₃₆ O ₂)	37.47	5.00
C18:2 (C ₁₉ H ₃₄ O ₂)	11.02	12.00

a group contribution method are implemented for the liquid specific heat capacity calculation [23]. The details of the estimation method are included in Ref. [21].

Table 2 illustrates the estimation methods used in the calculation of the FAME components for the PME-DM model. The PME-DM model is calculated using similar types of input to those used in the PME-CTM model. All the methods used to estimate the liquid properties in the simulation are the same for both the PME-CTM and PME-DM models as listed in Table 2 except the surface tension, the viscosity and the vapour pressure estimation methods. The Corresponding State, Orrick Erbar and Lee Kesler methods for surface tension, viscosity and vapour pressure are chosen based on recommendations in [37], which has compared various estimation methods with a reference database to determine the accuracy of each method.

The coefficients implemented in both models are compared in Table 5. The boiling point T_b for PME-CTM is about 5% lower than all the PME-DM fuel components because the boiling points that are implemented in both the models are based on published data from different sources [18,25].

Fig. 2(a)–(f) shows the comparison between the PME-CTM, PME-DM, and IDEA temperature dependent properties implemented in the present study. As shown in Table 5, C18:2 is the least volatile component which has about 20 K higher boiling point compared to the other three components which translates into a maximum of 60% difference in the vapour pressure as shown in Fig. 2(e). There is a significant difference between the vapour pressure profile of IDEA and that of the two PME models which agrees with the 40% higher measured initial boiling point of the biodiesel compared to that of diesel [25]. As expected, the vapour pressure profiles of PME-CTM and PME-DM follow similar trends and a larger difference between different components can be seen at high temperature. A similar trend can be seen in the latent heat of vaporisation profiles of FAME and PME-CTM shown in Fig. 2(d). The IDEA latent heat of vaporisation approaches an asymptote at a low boiling temperature while the PME-CTM and PME-DM latent heat of vaporisation decrease almost linearly towards the high temperature region. Both the vapour pressure and the latent heat of vaporisation are expected to have an effect on the predicted vaporisation behaviour of the fuel spray. The rest of the properties like density, surface tension, viscosity, and thermal conductivity show similar trends between PME-DM components and PME-CTM. As expected, Fig. 2(a)–(f) shows that IDEA has lower density, surface tension, and viscosity compared to PME.

All the properties mentioned in the present section are the only variables in the comparative cases that will be explained in Section 4. In order to see the effects of the fuel physical properties in isolation, vapour thermodynamic properties of heptane are used for all fuels, based on the standard OpenFOAM thermodynamics library.

3.4. Boundary conditions and uncertainties

The computational mesh for the reacting case consists of 70000 hexahedral cells in a cylindrical domain with swirl inlet and injector nozzle inlet at the bottom and an outlet at the top. The

cylindrical diameter and length are as shown in Fig. 1. An O-grid mesh is used to produce a hexahedral cell size of about 1 mm close to the injector nozzle with larger cells radially outwards. A mesh independence study has shown that a 2.5 mm cell size for the region far from the nozzle is sufficient for the gas phase.

The boundary conditions are set to emulate the experimental conditions [1,2]. The swirling air coming from the axial swirler is simulated using a velocity profile that consists of axial velocity U_z and tangential velocity U_t components. The axial velocity for the swirler inlet is calculated based on the air mass flow rate \dot{m}_{swirl} and the swirler geometry. The swirler tangential velocity $U_{t,swirl}$ is set based on Eq. (11) where the swirl number S_N is a function of the swirler geometry [30].

$$S_N = \frac{G_{m,axial}}{G_x R_{sw}} \quad (11)$$

Eq. (11) assumes conservation of the axial flux of angular momentum $G_m = f(U_{t,swirl}, U_{z,swirl}, r)$ and the axial flux of thrust G_x . The fuel mass flow rate and swirl air mass flow rate are set to preserve the experimental boundary condition. However, the atomising air mass flow rate could not be included at the injector nozzle location in the simulation due to the very small length scale of the atomiser nozzle (about 1 mm) in the present mesh setting and an unclear definition of the swirl intensity of the atomising air in the experiment [1,2]. The experimental atomising air mass flow rate is added to the swirl air mass flow rate boundary condition to maintain a global equivalence ratio $\Phi = 0.47$. The experimental combustor flow field that consists of a central recirculation zone and a corner recirculation zone [8] is well reproduced without the inclusion of the atomising air boundary condition.

A generic spray boundary condition is defined based on the Rosin–Rammler distribution function at the injector nozzle location to reproduce a spray penetration length that is comparable to the simulated flame height. A characteristic droplet diameter of 40 μm and a cone angle of 42° are defined at the spray boundary condition to produce a solid cone spray with the estimated mean injector velocity based on the experimental measurement [1,2]. A simulation with a comprehensive empirical boundary condition based on the droplet size and velocity measurement did not reproduce the experimental flame shape though the spray characteristics are predicted well [32].

Since an identical value of the enthalpy of combustion [26] is implemented for all the simulations, both the fuel mass flow rate and power output are fixed in the simulation. However, the two variables cannot be fixed in the experiment due to the difference in the lower heating value of diesel and biodiesel. The chemiluminescence data that is used in the present study is taken from different fuel spray flames at the same fuel mass flow rate. However, the (PDA) data is taken from measurements of different fuel spray flames at a varying fuel mass flow rate and fixed power output. No (PDA) data is available for flames having the same fuel mass flow for the different fuels. About 10% variation of fuel mass flow rate in the experiment is deemed quite acceptable for the present semi-quantitative validation of the spray characteristics.

Each case in the present study is run with a fixed time step. The injection velocity is set to be the same for each case, though the number of injected liquid parcels at each time step cannot be the same for each fuel because the number of injected liquid parcels is controlled by the fuel density. A sensitivity analysis is done to define the number of injected liquid parcels per time step for a satisfactory comparison between the cases. The convergence criterion is based on the convergence of the number of liquid parcels and the reduction of residuals below a set limit. Since the number of liquid parcels at steady state of the DM model shows more oscillation than that of the CTM model, the convergence time for the former is longer than that of the latter. Attention is given to

Table 5

Critical properties used in the calculation of the liquid properties in the PME-CTM and PME-DM models. The properties are calculated based on the Ambrose and Joback and the Lydersen and Ambrose methods respectively. The Lee Kesler mixing rule is applied for the PME-CTM model [13,37].

Liquid model	T_b (K)	T_c (K)	P_c (MPa)	V_c (m^3/kg)
C16:0	623	782	1.25	0.2742
C18:0	625	774	1.15	0.3361
C18:1	622	772	1.17	0.3279
C18:2	639	795	1.19	0.3219
PME-CTM	607	764	1.22	0.3400

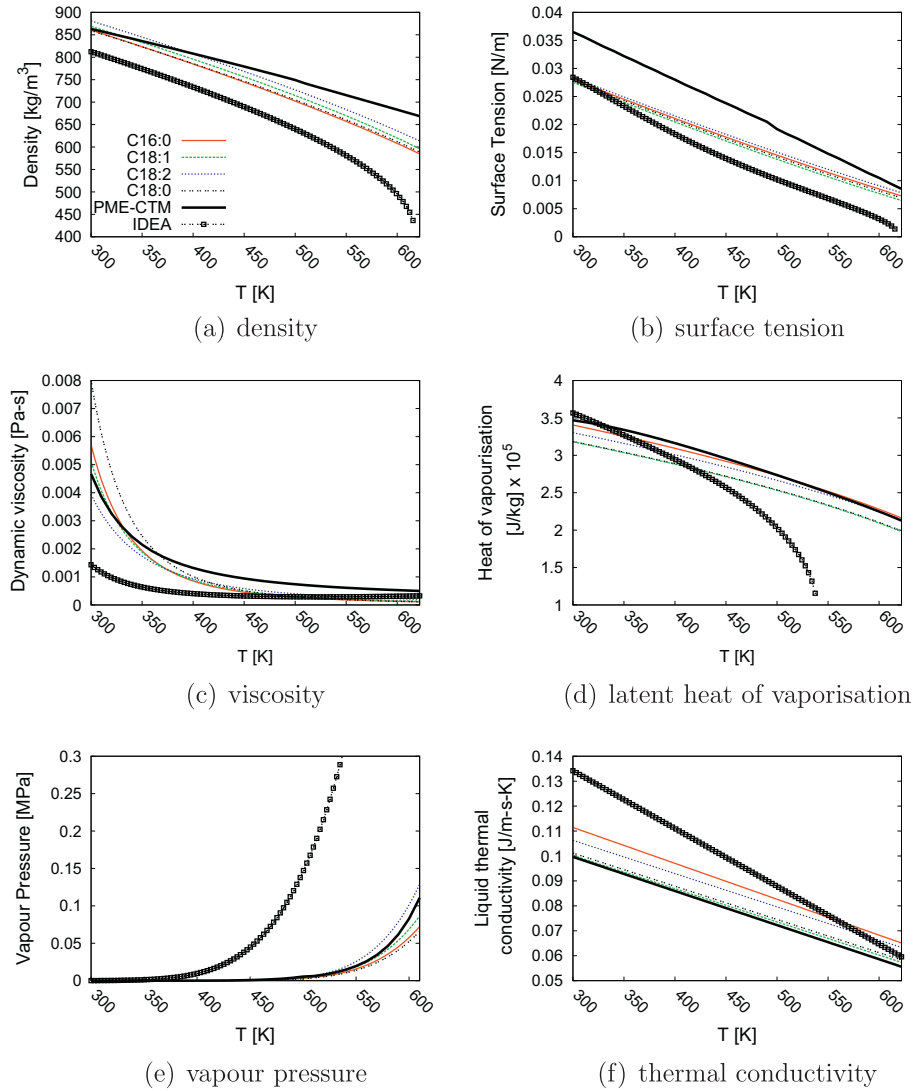


Fig. 2. FAME properties as implemented in the simulation code for the present study.

ensure that all the related results in the present study are representative average results of each case. For each simulation run, the average CPU time with 8 processors is 30 h on Intel Xeon® E5620 (2.4 GHz).

3.5. Lagrangian post-processor

In order to compare the present predicted spray characteristics with the (PDA) measurements that include the droplet size and the droplet velocity, a Lagrangian post-processor was developed. The Lagrangian computational parcel implemented in the simulation consists of a group of droplets that fall into a similar category in terms of size, velocity, and temperature.

$$N_i = \frac{M_i}{v_i \rho_d(T)_i} \quad (12)$$

Eq. (12) is used to calculate the number of droplets in each liquid parcel N_i , where M_i is the total mass of the i th computational parcel, v_i is the volume of one droplet in a parcel, and $\rho_d(T)_i$ is the temperature dependent density of the i th liquid parcel.

$$D_{32} = \frac{\sum N_i d_i^3}{\sum N_i d_i^2} \quad (13)$$

The calculation of the Sauter mean diameter D_{32} is done using Eq. (13) where d_i is the droplet size of the i th liquid parcel. The samples for the Sauter mean diameter calculation are taken at a cross section of the spray facing the direction of the flow at a certain sampling rate after the spray has reached convergence. The cross section sampling method is used for the mean droplet diameter and the mean droplet velocity \bar{U} calculation instead of a constant volume sampling method in order to get enough sample to reduce statistical noise. The liquid parcel axial velocity U_z , radial velocity U_r , and other scalars are averaged over the same samples. All the Lagrangian parameter prediction points have at least 1% of the total sample with a minimum number of 300 parcels to ensure statistical accuracy of the predictions.

If two non-evaporating spray cases of different fuels which have identical sizes and quantities are post processed using Eqs. (12) and (13), the calculated mean diameter can be different between the two cases due to the droplet density difference even though the physical breakup of the droplets never occurs in the simulation. Since the difference in the mean diameter in the non-evaporating spray case should be only due to the physical breakup of the droplets, this phenomenon is classified as an artificial effect of the density-dependent droplet number in a computational parcel. Therefore, an identical droplet density is used in

Eq. (12) for different fuels in the spray characteristic post-processing.

The volume flux F_{vol} is calculated based on Eq. (14) [31] at each respective radial location in the simulation. The droplet volumetric flow rate is given by $\dot{V}_d = \frac{\pi D_{30}^3}{6\Delta t}$ where $D_{30} = \left(\frac{\sum(N_i d_i^3)}{\sum(N_i)}\right)^{\frac{1}{3}}$ is the droplet volume mean diameter and Δt is the sampling period. The samples for volume flux are taken over a fixed cubic volume over a specified sampling time in the simulation and the probe area A_p is calculated based on the dimensions of the sampling volume.

$$F_{vol} = \frac{\dot{V}_d}{A_p} \quad (14)$$

A similar sampling approach is used for the droplet density F_{drop} which is calculated using Eq. (15) where V_p is the probe volume.

$$F_{drop} = \frac{\sum N_i}{V_p \Delta t} \quad (15)$$

4. Results

4.1. Combustion characteristics

Three different cases are compared which consist of IDEA, PME-DM, and PME-CTM. In all three cases, the liquid and the gas phase boundary conditions are kept constant. All the vapour properties are also fixed. The only variables in the three cases are the liquid properties as explained in Section 3.3. The validation is done based on a semi quantitative comparison using the two sets of experimental data of the diesel and the biodiesel flames.

The Abel transformed [38] OH* chemiluminescence of the two fuels is shown in Fig. 3(a) and (b). The direction of the spray is upwards and the swirling air coming from the same direction stabilises the flame near the nozzle. Both flames have similar height and flame lift off. The main reaction zone region on both sides of the two flames appears as a sheet structure in three dimensional space. As shown in Fig. 3(a), the biodiesel flame has a central top reaction zone (CTRZ) that joins the two sides of the reaction zone. The Abel transformed CTRZ which is rotated about the spray centreline creates a complete three dimensional structure near the top of the flame brush. The same phenomenon is quite weak in the diesel flame as shown in Fig. 3(b).

The predicted heat release rate per unit volume \dot{q} overlapped with the spray structure of the PME-CTM, PME-DM, and IDEA cases are shown in Fig. 3(c)–(e). The main two side reaction zones are reproduced in the simulation for both IDEA and PME with similar flame height as seen in the experiment (Fig. 3(a) and (b)). The flame lift-off is not within the scope of the present study and there has been no systematic effort to predict the flame lift off as observed in the experiment. The simulated flame height is 2 cm longer compared to the experimental observation. Fig. 3(c) and (e) show that the flame shapes are similar between PME-CTM and IDEA, which does not agree with the experimental observation as shown in Fig. 3(a) and (b). The CTRZ is not reproduced clearly with the PME-CTM model as seen in the contour plot of the heat release on the top flame brush in Fig. 3(c). The PME-DM model on the other hand produces a strong CTRZ as seen in Fig. 3(d) from the red contour in the CTRZ region. A longer spray penetration can be seen from the white dots representing the spray structure in the PME-DM case compared to that of IDEA, which agrees well with the experiment [1]. The same phenomenon is not predicted with the PME-CTM model. There is more interaction between droplets and flame and a thinner reaction zone in the PME-DM case compared to the IDEA and PME-CTM cases. Other experimental observations from single droplet studies also reveal a greater

tendency towards droplet-flame interaction for biodiesel compared to that of the more volatile fuel [10].

Fig. 4 shows the comparison of the measured centreline profile of the normalised OH* chemiluminescence intensity \hat{I} with respect to the predicted centreline profile of the normalised heat release rate per unit volume \hat{Q} . The quantity \hat{I} is defined as $\frac{I}{I_{max}}$ where I is the measured OH* intensity, and I_{max} is the maximum measured OH* intensity. The normalised heat release rate $\hat{Q} = \frac{\dot{q}}{\dot{q}_{max}}$ where \dot{q} is the predicted heat release rate and \dot{q}_{max} is the experimental combustor power output per unit volume. The normalised flame height is $\hat{Z} = \frac{z}{z_{max}}$ where z is the axial position and z_{max} is the estimated flame height which is determined based on a convenient value in the experiment and simulation to position the peak of \hat{I} and that of \hat{Q} at the same \hat{Z} location to facilitate the present comparison. $\hat{Z} = 0$ is the bottom of the flame, and $\hat{Z} = 1$ is an approximate flame height location. Since the centreline data of OH* chemiluminescence intensity is noisy, the centreline chemiluminescence intensity data shown in Fig. 4 has to be taken from an offset location which is about 3 mm from the actual centreline. The comparison between the diesel normalised OH* intensity \hat{I}_d and that of biodiesel \hat{I}_b indicates the increasing trend of heat release rate from the bottom of the flame to the CTRZ. The peak OH* intensity happens within the CTRZ, which is at about 65% of the flame height, before decreasing again towards the flame tip. Both the PME-CTM and PME-DM models capture the formation of the peak heat release rate within the CTRZ quite well. In the experiment, the peak of diesel OH* intensity is about a factor of 2 less than that of biodiesel OH* intensity as illustrated in Fig. 4. This again indicates that the biodiesel CTRZ heat release rate is higher in magnitude compared to that of the diesel. The PME-CTM model produces a trend which is not quite representative of the trend seen in the experiment, where the magnitude of the maximum heat release rate is similar to that of the IDEA-CTM model. By implementing the PME-DM model, the higher magnitude of the heat release rate for PME compared to that of IDEA is predicted as observed in the experiment.

Fig. 5 shows the predicted normalised fuel vapour mass fraction Y_{fuel} , normalised oxidiser mass fraction $Y_{oxidiser}$, and the normalised equivalence ratio $\hat{\phi}$ profiles on the spray centreline. The fuel vapour mass fraction is $Y_{fuel} = \frac{m_{fuel}}{m_g}$ where m_{fuel} and m_g are the fuel vapour mass and the total gas phase mass within the control volume respectively. The oxidiser mass fraction is $Y_{oxidiser} = \frac{m_{oxidiser}}{m_g}$ where $m_{oxidiser}$ is the oxygen mass within the control volume. The normalised equivalence ratio is $\hat{\phi} = \frac{\phi}{\phi_{max}}$ where ϕ is the predicted equivalence ratio and ϕ_{max} is the maximum predicted equivalence ratio based on the assumed heptane stoichiometry. The fuel vapour results for all three cases show an increasing trend with the maximum unburned fuel vapour present about halfway towards the CTRZ ($\hat{Z} = 0.3$) where oxidation occurs and the fuel vapour depletes within the CTRZ region. The effect of the higher volatility of IDEA compared to that of PME is seen in terms of about 20% difference in the fuel mass fraction near the bottom of the flames. The location of maximum IDEA fuel mass fraction happens further upstream compared to that of PME. It can be seen in the middle plot of Fig. 5 that PME-DM produces a longer fuel vapour penetration length compared to those of PME-CTM and IDEA resulting in a factor of three higher equivalence ratio compared to the other two cases, as seen in the top plot of Fig. 5. The large difference of equivalence ratio between PME-DM and PME-CTM is due to the oxidiser mass fraction in that region which is an order of magnitude lower than that of the fuel mass fraction. The fuel mass fraction and the oxidiser mass fraction axial profiles show the three dimensional behaviour of the flame which does not follow the classical one dimensional diffusion flame structure. The oxidiser mass fraction of all three cases is seen to decrease to a minimum value at the location of the maximum equivalence ratio before increasing again, which is partly due to the entrainment of the oxidiser from the

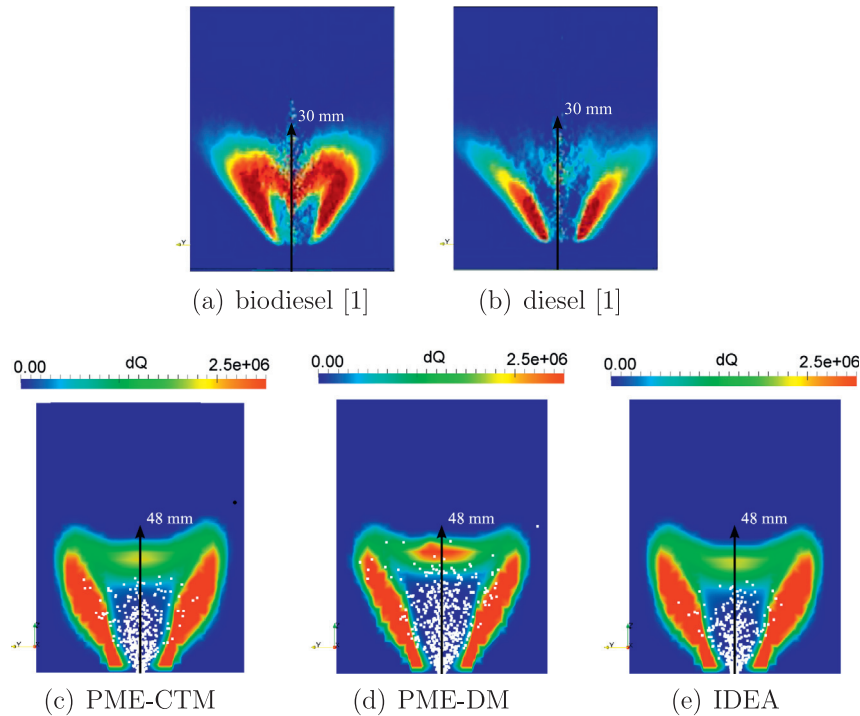


Fig. 3. Predicted heat release rate overlapped with the spray structures using different liquid models and Abel transformed OH* chemiluminescence images [1] using different fuel sprays.

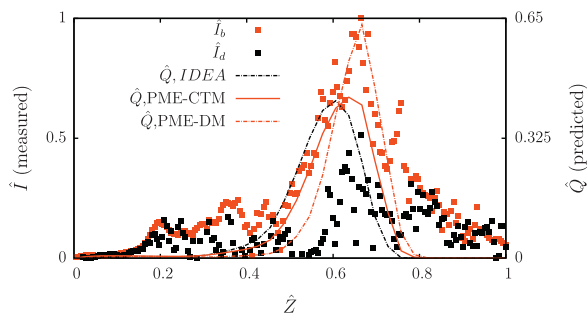


Fig. 4. Comparison of the normalised heat release rate \dot{Q} with the normalised OH* chemiluminescence intensity I on the centreline

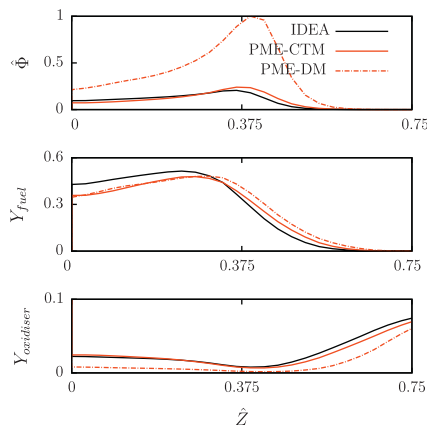


Fig. 5. The centreline profile of the normalised equivalence ratio $\hat{\phi}$, the fuel vapour mass fraction Y_{fuel} , and the oxidiser mass fraction $Y_{oxidiser}$.

swirling air into the core of the central recirculation zone. The difference in the heat release rate profile of PME-DM and that of PME-CTM causes differences in the flow field which in turn cause a marked difference in the oxidiser mass fraction between the two cases. As a result of the increase in the PME-DM local equivalence ratio at $\hat{Z} = 0.65$, a mixture which is closer to stoichiometric is produced (given that the local equivalence ratio is on the lean side) and a 30% higher magnitude of PME-DM heat release rate compared to that of IDEA is predicted in that region, as seen in Fig. 4. The same phenomenon is not reproduced with the PME-CTM case even though initially, the magnitude of the fuel vapour mass fraction of both PME cases is similar from the bottom of the flame up to $\hat{Z} = 0.3$ as seen in the middle plot of Fig. 5. It can be verified based on the present comparison that the formation of the strong CTRZ that is seen in the experimental biodiesel flame is as a result of the formation of combustible mixture due to the longer fuel vapour penetration of the biodiesel spray compared to that of diesel. The slower evaporation rate of biodiesel spray compared to that of diesel spray is captured with the PME-DM model due to the survival of less volatile and more abundant components.

The profile of the fuel vapour components mass fraction Y_i at the centreline of the PME-DM flame is shown in Fig. 6. The fuel vapour components mass fraction Y_i is defined as $\frac{m_i}{m_g}$, where m_i is the fuel vapour component mass within the control volume. Mass conservation of the PME-DM fuel vapour can be verified by confirming that the integral of the vapour components mass fraction profile over the flame height for all FAME components in Fig. 6 should equal the same integral for the PME-DM curve in Fig. 5. Similar to the PME-DM fuel vapour mass fraction trend, the fuel components mass fraction trend shows a maximum point at about the same place, with a slight shift in the location of the maximum mass fraction of the less volatile fuel components. C16:0 which is the most abundant component and the second least volatile component is seen to penetrate the most into the CTRZ region followed

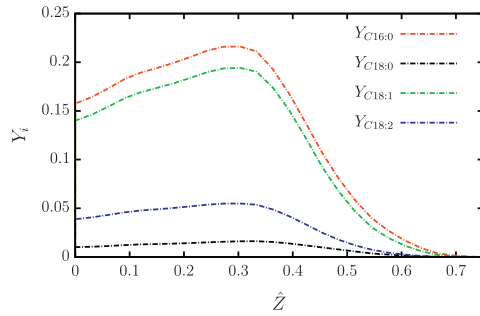


Fig. 6. Centreline profile of the fuel vapour components mass fraction Y_i in the PME-DM flame.

by C18:1, C18:2, and C18:0. This trend illustrates that the relative abundance of the components dominates over their relative volatility in the multicomponent biodiesel fuel vapour formation. In the literature, an emphasis has been given to the latter effect in non-reacting multicomponent spray evaporation [35], but the present reacting spray study highlights the influence of the former. For the present case of PME, the smallest methyl ester component C16:0 in the composition is seen to have the longest penetration. This phenomenon might differ in the case of biodiesel derived from other sources that have different FAME composition. A validation of the DM model based on an evaporating biodiesel droplet has been done elsewhere [33] in the absence of combustion.

4.2. Spray characteristics

Fig. 7(a)–(c) shows the radial profile validation of the normalised Sauter mean diameter \hat{D}_{32} , the normalised volume flux \hat{V} , and the normalised droplet density \hat{D} . All the spray variables are normalised with their respective maximum values except \hat{D}_{32} which is normalised with the characteristic diameter δ which is

used in the Rosin Rammler distribution function in the spray boundary condition specification. The normalised radial location \hat{r} is defined as $\frac{r}{r_{ch}}$, where r_{ch} is a characteristic radial location used to indicate the radial extent of the spray at a particular radial location. The characteristic radial location is adjusted to match the location of the maximum of the predictions with that of the measurements to facilitate the comparison of the maximum values of the two sets of variables. The predicted maximum volume flux is offset by 5 mm compared to the measured maximum volume flux location before the normalisation. On average, the droplet size, volume flux, and droplet density of biodiesel is 20% higher compared to that of diesel in the experiment. The large discrepancy is due to the use of the generic spray boundary condition based on the reproduction of the spray penetration in the experiment. From a separate sensitivity analysis, the predicted spray characteristics are strongly influenced by the spray boundary condition. Since the droplet size measurement is taken at 10 mm downstream of the nozzle which is almost half the flame height [2], the data cannot be used to define the spray boundary condition.

The reproduction of the experimental trends of quasi-uniform droplet size, and non-uniform volume flux and droplet density profiles is quite satisfactory in the simulation as seen in Fig. 7(a)–(c). However, due to the inherent limitation of the present generic spray boundary condition which provides no control over the spatial variation of the injected droplet size, the increasing droplet size in the radial direction that is seen in the experiment [1,2] is not reproduced in the simulation, as seen in Fig. 7(a). A higher droplet size, volume flux and droplet density of biodiesel compared to that of diesel is also reproduced in the simulation with a satisfactory magnitude of the difference between the two fuels. Both PME-DM and PME-CTM provide similar droplet size and volume flux predictions. The droplet density of PME-DM is about 25% higher compared to that of PME-CTM due to the higher vaporisation rate of the latter which causes the PME-CTM droplets to be destroyed at a higher rate. From Fig. 7(c), the PME-DM droplet density prediction is marginally more accurate compared to that of PME-CTM

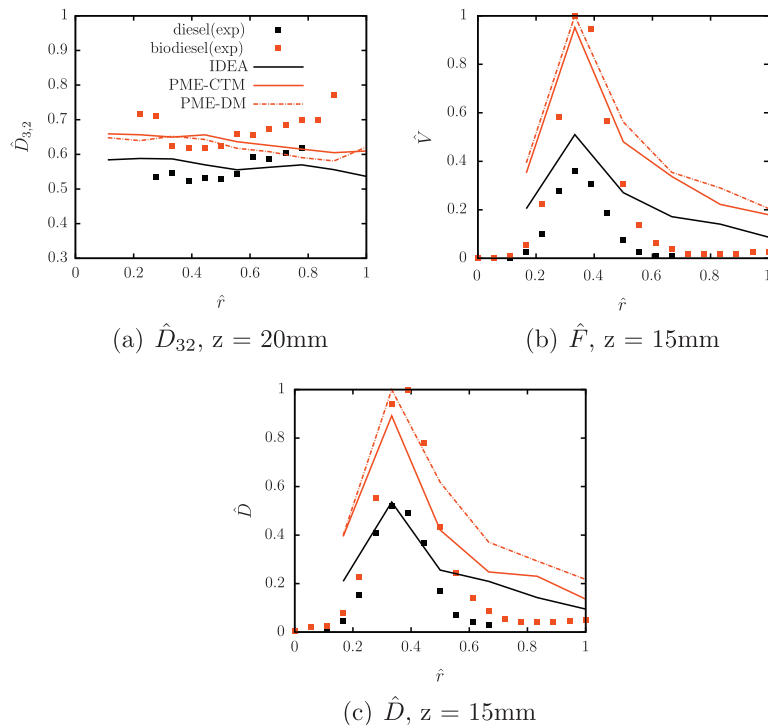


Fig. 7. The radial profiles of the normalised Sauter mean diameter D_{32} , the normalised volume flux V , and the normalised droplet density D .

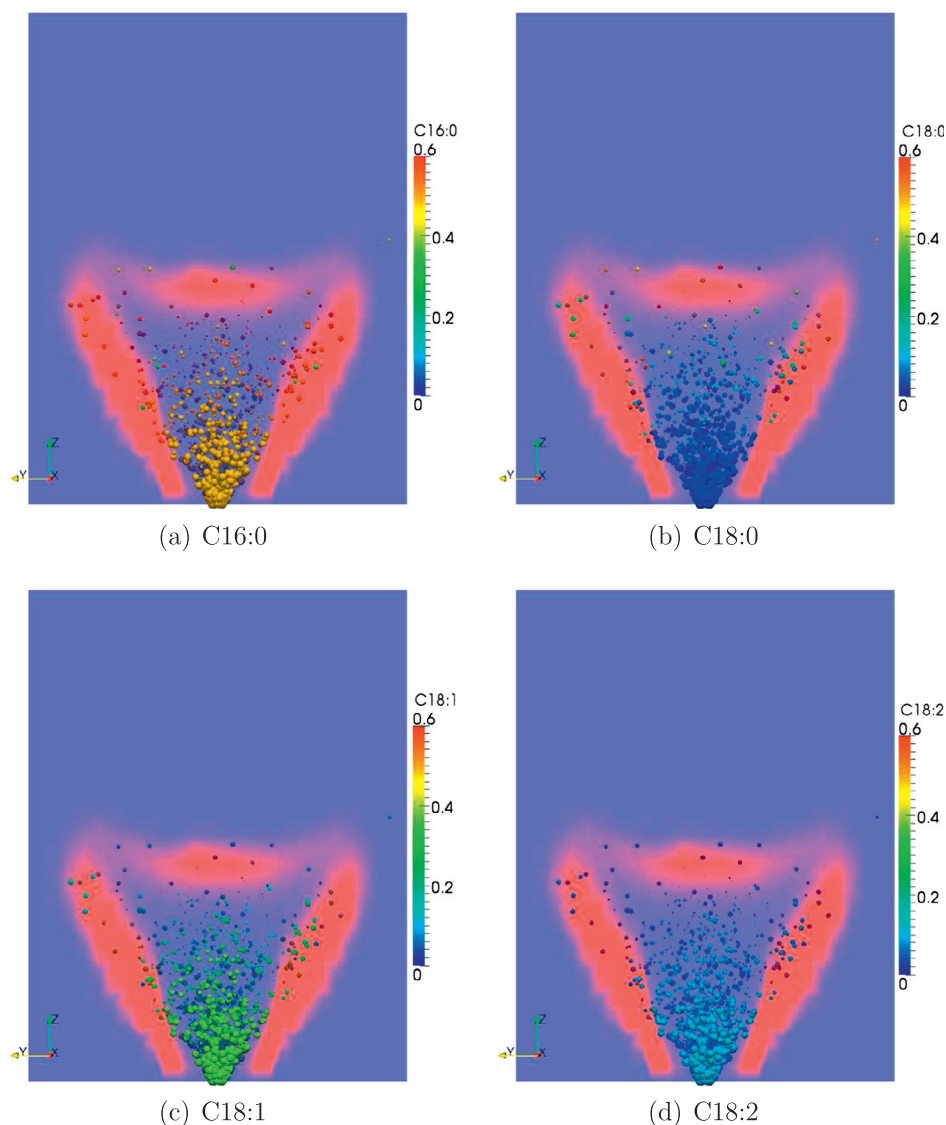


Fig. 8. PME-DM spray structures overlapped with the reaction zones. The colour bars represent the liquid mass fractions of the pure components and the droplets sizes represent the velocities. (For interpretation of the references to colour in this figure legend, the reader is referred to the web version of this article.)

in terms of producing the desired higher droplet density compared to IDEA as observed in the experiment. The difference between the two models cannot be shown in terms of the droplet size and the volume flux profiles due to the effect of averaging in the calculation of the two variables.

Fig. 8(a)–(d) illustrate the solid cone spray structure of PME-DM overlapped with the reaction zone. The droplets are sized based on velocities and coloured based on the component mass fraction. The droplet velocity reduction can be seen as the droplets experience ambient gas drag as they travel downstream into the reaction zone. Within the core of the spray near the nozzle, the liquid consists of mainly C16:0 followed by the less abundant components C18:1, C18:2, and C18:0. This trend is explained by the mass percentage profile of PME-DM discussed in Section 3.3. As the spray travels downstream, the more volatile components like C18:1 evaporate more rapidly than C16:0 which causes the C18:1 mass fraction to reduce as shown in Fig. 8(c). On the other hand, Fig. 8(a) shows that the less volatile component C16:0 evaporates less rapidly and its mass fraction within the spray increases as the spray travels downstream. Similar comparisons can be made between C18:0 and C18:2 as shown in Fig. 8(b) and (d).

5. Conclusion

A swirl stabilised flame of biodiesel is simulated in OpenFOAM using real biodiesel physical properties and both the CTM and DM models. A diesel flame is simulated using simplified diesel properties based on the CTM model only. The DM model takes into account the relative abundance and the relative volatility of the fuel components. The vapour thermodynamic properties and the chemical reaction mechanism are kept the same for both fuels to allow a study of the effects of fuel physical properties in isolation. A semi-quantitative validation is done based on experimental measurements of the OH^* chemiluminescence intensity and the spray characteristics in order to investigate the accuracy of the modelling approach.

A simple change to the modelling of the fuel physical properties as implemented in the PME-DM method allows the prediction of a longer biodiesel spray penetration length compared to that of diesel. A clear central top reaction zone is predicted for the biodiesel flame using the PME-DM model, due to the formation of a combustible mixture near the top of the flame brush. The same phenomenon is not reproduced with the PME-CTM model. In the biodiesel

spray flame, the relative abundance of each fuel component dominates over the relative volatility in the formation of the segregated fuel vapour field. The opposite effect is seen in the formation of the segregated liquid vapour field. Both the PME-DM and the PME-CTM methods predict larger droplet size, volume flux, and droplet density for the biodiesel spray compared to the diesel spray. The PME-DM prediction of droplet density is marginally more accurate than that of the PME-CTM model. Overall, the PME-DM model performs better than the PME-CTM model in simulating the spray-combustion behaviour of a composite fuel like biodiesel.

Acknowledgements

This work is financially supported by the Ministry of Science, Technology & Innovation, Malaysia (MOSTI) and Universiti Teknologi Malaysia (UTM). Permission to use the BDProp software from Prof. A. Hansen (University of Illinois - Urbana Champaign) and Dr. W. Yuan (Kansas State University) is highly appreciated.

References

- [1] Chong C, Hochgreb S. Combustion characteristics of alternative liquid fuels. PhD thesis, University of Cambridge; 2011.
- [2] Chong C, Hochgreb S. Spray combustion characteristics of palm biodiesel. *Combust Sci Technol* 2012;184:1093–107.
- [3] Hashimoto N, Ozawa Y, Mori N, Yuri I, Hisamatsu T. Fundamental combustion characteristics of palm methyl ester (PME) as alternative fuel for gas turbines. *Fuel* 2008;87:3373–8.
- [4] Yamane K, Ueta A, Shimamoto Y. Influence of physical and chemical properties of biodiesel fuels on injection, combustion and exhaust emission characteristics in a direct injection compression engine. *Int J Engine Res* 2001;2:249–61.
- [5] Bolszo C, McDonnell V, Samuelsen S. Impact of biodiesel on fuel preparation and emissions for a liquid fired gas turbine engine. *ASME Turbo Expo GT2007-27652*; 2007.
- [6] Sequera D, Agrawal K, Scott K, Daniel T. Combustion performance of liquid bio-fuels in a swirl stabilized burner. *ASME Turbo Expo GT2007-28326*; 2007.
- [7] Chong C, Hochgreb S. Measurements of laminar flame speeds of liquid fuels: Jet-A1, diesel, palm methyl esters and blends using particle imaging velocimetry (PIV). *Proc Combust Inst* 2011;33:979–86.
- [8] Chong C, Hochgreb S. Flow field of a model gas turbine swirl burner. *Adv Mater Res* 2013;622:1119–24.
- [9] Jha S, Fernando S, To S. Flame temperature analysis of biodiesel blends and components. *Fuel* 2008;87:1982–8.
- [10] Gordon RL, Mastorakos E. Autoignition of monodisperse biodiesel and diesel sprays in turbulent flows. *Exp Therm Fluid Sci* 2012;43:40–6.
- [11] Golovitchev VI, Yang J. Construction of combustion models for rapeseed methyl ester bio-diesel fuel for internal combustion engine application. *Biotechnol Adv* 2009;27:641–55.
- [12] Rochaya D. Numerical simulation of spray combustion using bio-mass derived liquid fuels. PhD thesis, Cranfield University; 2007.
- [13] Yuan W. Computational modeling of NOx emission from biodiesel combustion based on accurate fuel properties. PhD thesis, University of Illinois; 2005.
- [14] Mohamed Ismail H, Ng HK, Cheng X, Gan S, Lucchini T, D'Errico G. Development of thermophysical and transport properties for the CFD simulations of in-cylinder biodiesel spray combustion. *Energy Fuels* 2012;26:4857–70.
- [15] Prussi M, Chiaramonti D, Riccio G, Martelli F, Pari L. Straight vegetable oil use in micro-gas turbines: system adaptation and testing. *Appl Energy* 2012;89:287–95.
- [16] Barata J. Modelling of biofuel droplets dispersion and evaporation. *Renew Energy* 2008;33:769–79.
- [17] Ra Y, Reitz RD, McFarlane J, Daw C. Effects of fuel physical properties on diesel engine combustion using diesel and bio-diesel fuels. *SAE Int J Fuels Lubricants* 2008;1:703–8.
- [18] Graboski MS, McCormick RL. Combustion of fat and vegetable oil derived fuels in diesel engines. *Progr Energy Combust Sci* 1998;24:125–64.
- [19] Choi C, Reitz RD. A numerical analysis of the emissions characteristics of biodiesel blended fuels. *J Eng Gas Turb Power* 1999;121:31–7.
- [20] Yuan W, Hansen AC. Computational investigation of the effect of biodiesel fuel properties on diesel engine NOx emissions. *Int J Agric Biol Eng* 2009;2:41–8.
- [21] Yuan W, Hansen AC, Zhang Q. Predicting the physical properties of biodiesel for combustion modeling. *Trans Am Soc Agric Eng* 2003;46:1487–93.
- [22] Huber M, Perkins RA. Thermal conductivity correlations for minor constituent fluids in natural gas: n-octane, n-nonane and n-decane. *Fluid Phase Equilib* 2005;227:47–55.
- [23] Fisher EM, Pitz WJ, Curran HJ, Westbrook CK. Detailed chemical kinetic mechanism for combustion of oxygenated fuels. *Proc Combust Inst* 2000;28:1579–86.
- [24] Crocker D, Widmann J, Presser C. CFD modeling and comparison with data from the NIST reference spray combustor. *Am Soc Mech Eng Heat Transfer Div* 2001;4:81–90.
- [25] Benjumea P, Agudelo JI, Agudelo A. Basic properties of palm oil biodiesel and diesel blends. *Fuel* 2008;87:2069–75.
- [26] <ftp://ftp.technion.ac.il/pub/supported/aetdd/thermodynamics/>.
- [27] Karrholm P. Numerical modelling of diesel spray injection, turbulence interaction and combustion. PhD thesis, Chalmers University of Technology; 2008.
- [28] Westbrook CK, Dryer FL. Simplified reaction mechanisms for the oxidation of hydrocarbon fuels in flames. *Combust Sci Technol* 1981;27:31–43.
- [29] Hentschel W, Schindler K, Haahtela O. European diesel research IDEA-experimental results from DI diesel engine investigations, SAE paper 941954; 1994.
- [30] Beer J, Chigier NA. *Combustion aerodynamics*. Krieger; 1972.
- [31] Widmann J, Presser C, Giridharan M, Crocker D. Issues related to spray combustion modelling validation. *AIAA* 2001-0363; 2001.
- [32] Mohd Yasin M, Cant S, Chong C, Hochgreb S. Effects of the biodiesel fuel physical properties on the swirl stabilised spray combustion characteristics. SAE paper 2012-01-1724; 2012.
- [33] Zhang L, Kong S. Vaporization modeling of petroleum-biofuel drops using a hybrid multi-component approach. *Combust Flame* 2010;157:2165–74.
- [34] Zhang L, Kong S. High-pressure vaporization modeling of multi-component petroleum and biofuel mixtures under engine conditions. *Combust Flame* 2011;158:1705–17.
- [35] Zhang L, Kong S. Multicomponent vaporization modeling of bio-oil and its mixtures with other fuels. *Fuel* 2012;95:471–80.
- [36] Gu X, Basu S, Kumar R. Dispersion and vaporization of biofuels and conventional fuels in a crossflow pre-mixer. *Int J Heat Mass Transfer* 2012;55:336–46.
- [37] An H, Yang W, Maghbouli A, Chou SK, Chua KJ. Detailed physical properties prediction of pure methyl esters for biodiesel combustion modeling. *Appl Energy* 2012;102:647–56.
- [38] Won SH, Lee JS, Jin SH, Chung SH. Visualization of lifted laminar jet flame by rayleigh scattering, OH PLIF, and CH chemiluminescence. *J Visualization* 2003;6:211–31.